Available online at www.sciencedirect.com
ScienceDirect
International Journal of Heat and Mass Transfer 50 (2007) 348–360
International Journal of HEAT and MASS TRANSFER
www.elsevier.com/locate/ijhmt

Effects of gravity modulation on convection in a horizontal annulus

Mark P. Dyko [a], Kambiz Vafai [b,*]

[a] Research and Technology, Aircraft Braking Systems Corporation, Akron, Ohio 44306, United States
[b] Department of Mechanical Engineering, University of California, A363 Bourns Hall, California, Riverside, CA 92521-0425, United States

Received 13 April 2006; received in revised form 10 June 2006
Available online 6 September 2006

Abstract

Convection in the annulus between two horizontal coaxial cylinders resulting from gravity modulation in a microgravity environment is investigated for the first time. The three-dimensional transient equations of fluid motion and heat transfer are solved to study the unsteady flow structures in a large-gap annulus. The gravity fluctuations are shown to induce recirculating flows that reverse direction of rotation in response to the gravitational reversals. Except for a short period of time following flow reversal, at low modulation frequencies the centers of rotation of these flows are below and above the horizontal angular plane when the acceleration acts in the upward and downward directions, respectively, whereas at high frequencies they are above and below this plane. The effects of gravity modulation on development of secondary flows that arise in narrow- and moderate-gap annuli owing to thermal instability are also investigated. It is found that supercritical transverse rolls repeatedly form, dissipate, and re-form in the upper and lower regions of a narrow-gap annulus as a result of the fluctuating gravity field. At the same frequency, the supercritical rolls in a moderate-gap annulus are much slower to develop between flow reversals. The results show that gravity modulation has a stabilizing effect on the secondary flows compared to the case of a constant gravity force, and this effect diminishes with reduction in either frequency or annulus radius ratio R. The effects of frequency on heat transfer in large-, moderate-, and narrow-gap annuli are also studied. It is found that the time-averaged Nusselt number approaches that of pure conduction at high frequencies and increases toward that for terrestrial natural convection as frequency is reduced. As R is decreased, the increase in time-averaged Nusselt number brought about by reducing frequency becomes a smaller percentage of the value for terrestrial natural convection. The results for large-, moderate-, and narrow-gap annuli subjected to gravity modulation under microgravity are compared to results for steady natural convection under terrestrial conditions to clarify differences in flow behavior. The present work provides the first description of convection in a cylindrical annulus under microgravity, and practical information on the influence of gravity fluctuations on heat transfer in a space environment.

Keywords: Gravity modulation; Microgravity; *g*-jitter; Horizontal annulus; Buoyancy-induced convection

1. Introduction

Buoyancy-driven convection in microgravity resulting from gravity fluctuations has gained considerable attention owing to the possibility of conducting research in the low-gravity environment of space, and because of interest in the fundamental effects of gravity modulation on fluid systems. On spacecraft, fluctuating accelerations can originate from a variety of sources such as crew activities, vibrations from onboard equipment, and structural oscillations of the spacecraft. Typical peak g levels, although small relative to terrestrial gravity [1], are at least 100 times larger than the steady g levels in space. The fluctuating accelerations act on density gradients in the fluid caused by heat and/or mass transfer between the fluid and boundaries, producing convective motions. These motions may increase heat transfer significantly beyond that of pure conduction, and can strongly affect certain processes such as alloy solidification.

Previous studies of buoyancy-induced fluid motion and heat transfer resulting from gravity modulation under microgravity have focused on a few basic fluid systems, as well as some specific applications. Kamotani et al. [2] conducted a linearized numerical analysis for a

* Corresponding author. Tel.: +1 951 827 2135; fax: +1 951 827 2899.
E-mail address: vafai@engr.ucr.edu (K. Vafai).

0017-9310/$ - see front matter © 2006 Elsevier Ltd. All rights reserved.
doi:10.1016/j.ijheatmasstransfer.2006.06.033

Nomenclature

A	annulus gap aspect ratio $= l/(r_o - r_i)$
g	gravitational acceleration
g_o	constant gravity level in space
g'	amplitude of oscillating component of acceleration
l	annulus length
L	dimensionless annulus length $= l/r_i$
$\overline{Nu}_{ai}$	inner cylinder angular mean Nusselt number
$\overline{Nu}_{ao}$	outer cylinder angular mean Nusselt number
Pr	Prandtl number $= \nu/\alpha$
r	dimensionless radial coordinate $= r^*/r_i$
r_i	inner cylinder radius
r_o	outer cylinder radius
R	annulus radius ratio $= r_o/r_i$
Ra	Rayleigh number based on annular gap width $= g\beta(r_o - r_i)^3\Delta T/\alpha\nu$
Ra_r	Rayleigh number based on inner cylinder radius $= g\beta r_i^3\Delta T/\alpha\nu$
t	dimensionless time $= t^*\alpha/r_i^2$
T	temperature
ΔT	temperature difference $= T_i - T_o$
T_i	inner cylinder temperature
T_o	outer cylinder temperature
V	dimensionless velocity $= V^* r_i/\alpha$
$\boldsymbol{V}$	velocity vector
z	dimensionless axial coordinate $= z^*/r_i$

Greek symbols

α	thermal diffusivity
β	thermal expansion coefficient
ϕ	angular coordinate
λ	thermal conductivity
ν	kinematic viscosity
Θ	dimensionless temperature $= (T - T_o)/\Delta T$
ρ	density
ω	frequency of gravitational oscillation
$\boldsymbol{\Omega}$	vorticity vector
$\boldsymbol{\Psi}$	vector potential

Subscripts

a	angular
i	inner cylinder
o	outer cylinder
r	radial component
ϕ	angular component
z	axial component

Superscript

*	dimensional quantity

two-dimensional rectangular enclosure with two opposing walls at unequal temperatures. They concluded that modulation normal to the direction of the temperature gradient is most critical. Amin [3] analytically studied heat transfer from a sphere. It was concluded that for high modulation frequencies heat transfer is negligible, while for low frequencies heat transfer will be non-trivial for fluids of small viscosity and sufficiently large Prandtl number. The effects of non-linearity of the governing equations for the rectangular enclosure problem were investigated by Biringen and Danabasoglu [4]. They established some limits on applicability of the linear models in the excitable frequency range. Biringen and Peltier [5] considered the effects of three-dimensionality as well as non-linearity of the governing equations for both sinusoidal and random modulations. They found that sinusoidal modulations are more stabilizing than random modulations, and the similarity between terrestrial systems and systems at low-gravity increases with increasing modulation amplitude. Cyr et al. [6] also conducted a numerical study of convection in a two-dimensional rectangular enclosure. Their results showed that the flow transitions from stable, to periodic, to non-periodic behavior as the frequency of the modulation is varied. The average heat transfer rate was found to increase significantly as the frequency was decreased to low values. Other investigations have been conducted to determine the effects of gravity modulation on melt processing systems in microgravity [7–9].

A problem that has been widely studied owing to its many practical applications is natural convection in the annulus between horizontal concentric cylinders. Depending on the outer to inner cylinder radius ratio R and the Rayleigh number, various types of laminar flow structures can arise in a sufficiently long horizontal annulus. Based on their experimental results and those of previous investigators, Powe et al. [10] classified various types of laminar natural convective regimes as (i) a unicellular steady regime for small Rayleigh numbers at any value of R, (ii) a multicellular regime for higher Rayleigh numbers and $R < 1.24$ (narrow-gap annulus), (iii) a spiral flow regime for higher Rayleigh numbers and R between 1.24 and 1.71 (moderate-gap annulus), and (iv) an oscillating regime for higher Rayleigh numbers and $R > 1.71$ (large-gap annulus). Most of the prior studies of buoyancy-induced convection in horizontal cylindrical annuli have dealt with two-dimensional flow occurring in annuli with large length to gap-thickness ratios. There are fewer studies of three-dimensional flow, which occurs owing to the presence of the endwalls or the onset of instabilities at higher Rayleigh numbers. Previous numerical studies of three-dimensional natural convection in large- and moderate-gap annuli have focused on

classification of different convective regimes [11], the effects of annulus inclination [12], flow patterns in a short annulus [13], temporal development of the flow and temperature fields [14], turbulent flow [15], and high Rayleigh number laminar flow [16]. Three-dimensional buoyancy-driven convection in a narrow-gap annulus has been investigated by Dyko and Vafai [17]. The results of this study showed the existence of four different supercritical states characterized by the orientations and directions of rotation of counter-rotating convective rolls that form in the upper part of the annulus owing to thermal instability. A fifth supercritical state was studied by Dyko and Vafai [18].

In the present work, we extend the problem of buoyancy-induced convection in horizontal annuli to the case of gravity modulation in a microgravity environment, which has application to systems such as materials processing furnaces. In this three-dimensional numerical investigation, the governing equations are formulated in terms of vorticity and vector potential. The parabolic equations are solved by a three-dimensional three-level time-splitting ADI method, and the elliptic equations are solved by the extrapolated Jacobi method. The flow structures that arise in large-, moderate-, and narrow-gap annuli under microgravity as a result of periodic gravity modulation, and the influence of modulation frequency on the flow and heat transfer are presented.

2. Physical model

2.1. Governing equations and solution

The inner and outer horizontal concentric cylinders have radii of r_i and r_o, respectively, and are of length l. The temperature of the inner cylinder T_i is greater than that of the outer cylinder T_o, and the two axial endwalls are impermeable and adiabatic. The dimensionless length of the annulus is defined as $L = l/r_i$. The annulus geometry, which is characterized by the radius ratio $R = r_o/r_i$ and gap aspect ratio $A = l/(r_o - r_i)$, is shown in Fig. 1. In all of the numerical simulations, the computational domain was chosen to encompass the full radial ($1 \leqslant r \leqslant R$), angular ($-\pi \leqslant \phi \leqslant \pi$), and axial ($0 \leqslant z \leqslant L$) extent of the annulus.

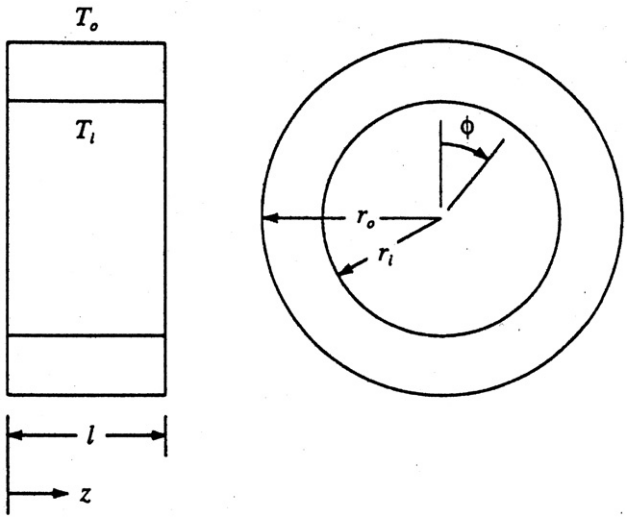

Fig. 1. Schematic diagram of the cylindrical annulus.

The transient, three-dimensional, laminar, buoyancy-induced flow of an incompressible, Newtonian fluid is governed by the equations of conservation of mass, momentum, and energy. The momentum equation is simplified using the Boussinesq approximation. For the purpose of illustrating the fundamental effects of gravity modulation on flow and heat transfer, and to facilitate comparison of the results to those for natural convection under terrestrial conditions, a unidirectional gravitational field with sinusoidal oscillation is assumed. The components of the gravitational vector in the r, ϕ, and z directions are $-g\cos\phi\,\mathbf{e_1}$, $g\sin\phi\,\mathbf{e_2}$, and 0, respectively, where g denotes the time-dependent gravitational acceleration and $\mathbf{e_1}$, $\mathbf{e_2}$, and $\mathbf{e_3}$ are the unit vectors in cylindrical coordinates. The gravitational acceleration is expressed as $g = g_o + g'\sin(\omega t)$, where g_o is the constant gravity level in space, g' is the amplitude of the oscillating component of acceleration, and ω is the frequency of the gravitational oscillation. It is noted the direction of gravitational acceleration is parallel to the temperature gradient at angular locations $\phi = 0$, π (upper and lower vertical angular planes), and perpendicular to the temperature gradient at locations $\phi = \pi/2$, $-\pi/2$ (horizontal angular planes). At other angular locations, the direction is neither parallel nor perpendicular to the temperature gradient.

The pressure term is eliminated by taking the curl of the momentum equation, which yields the equations for transport of vorticity

$$\frac{\partial \Omega_r}{\partial t} + (\boldsymbol{V}\cdot\nabla)\Omega_r - (\boldsymbol{\Omega}\cdot\nabla)V_r = Pr\left(\nabla^2\Omega_r - \frac{\Omega_r}{r^2} - \frac{2}{r^2}\frac{\partial \Omega_\phi}{\partial \phi}\right) + PrRa_r\sin\phi\frac{\partial \Theta}{\partial z} \tag{1}$$

$$\frac{\partial \Omega_\phi}{\partial t} + (\boldsymbol{V}\cdot\nabla)\Omega_\phi - (\boldsymbol{\Omega}\cdot\nabla)V_\phi + \frac{V_\phi\Omega_r - V_r\Omega_\phi}{r} = Pr\left(\nabla^2\Omega_\phi - \frac{\Omega_\phi}{r^2} + \frac{2}{r^2}\frac{\partial \Omega_r}{\partial \phi}\right) + PrRa_r\cos\phi\frac{\partial \Theta}{\partial z} \tag{2}$$

$$\frac{\partial \Omega_z}{\partial t} + (\boldsymbol{V}\cdot\nabla)\Omega_z - (\boldsymbol{\Omega}\cdot\nabla)V_z = Pr\nabla^2\Omega_z - Pr\ Ra_r\left(\sin\phi\frac{\partial \Theta}{\partial r} + \frac{1}{r}\cos\phi\frac{\partial \Theta}{\partial \phi}\right) \tag{3}$$

where the vorticity vector is defined by $\boldsymbol{\Omega} = \nabla \times \boldsymbol{V}$. The vector potential $\boldsymbol{\Psi}$ is introduced for satisfying the conservation of mass and calculation of the velocity field from the vorticity field, where $\boldsymbol{V} = \nabla \times \boldsymbol{\Psi}$. From the equations defining vorticity and vector potential, and imposing the solenoidal condition $\nabla\cdot\boldsymbol{\Psi} = 0$, the equation $-\boldsymbol{\Omega} = \nabla^2\boldsymbol{\Psi}$ relating vector potential and vorticity is obtained, which is written as

$$-\Omega_r = \nabla^2 \Psi_r + \frac{2}{r}\frac{\partial \Psi_r}{\partial r} + \frac{\Psi_r}{r^2} + \frac{2}{r}\frac{\partial \Psi_z}{\partial z} \tag{4}$$

$$-\Omega_\phi = \nabla^2 \Psi_\phi - \frac{\Psi_\phi}{r^2} + \frac{2}{r^2}\frac{\partial \Psi_r}{\partial \phi} \tag{5}$$

$$-\Omega_z = \nabla^2 \Psi_z \tag{6}$$

From the definition of vector potential, the components of velocity are

$$V_r = \frac{1}{r}\frac{\partial \Psi_z}{\partial \phi} - \frac{\partial \Psi_\phi}{\partial z} \tag{7}$$

$$V_\phi = \frac{\partial \Psi_r}{\partial z} - \frac{\partial \Psi_z}{\partial r} \tag{8}$$

$$V_z = \frac{\Psi_\phi}{r} + \frac{\partial \Psi_\phi}{\partial r} - \frac{1}{r}\frac{\partial \Psi_r}{\partial \phi} \tag{9}$$

Eqs. (1)–(9) along with the energy Eq. (10) are solved for the ten unknowns: Ω_r, Ω_ϕ, Ω_z, Ψ_r, Ψ_ϕ, Ψ_z, V_r, V_ϕ, V_z and Θ.

$$\frac{\partial \Theta}{\partial t} + (\mathbf{V}\cdot\nabla)\Theta = \nabla^2 \Theta \tag{10}$$

The conservation equations were non-dimensionalized using r_i for length, α/r_i for velocity, r_i^2/α for time and $\rho\alpha^2/r_i^2$ for pressure, with α and ρ denoting the thermal diffusivity and density, respectively. The dimensionless temperature is defined by $\Theta = (T - T_o)/\Delta T$, where $\Delta T = T_i - T_o$. The dimensionless parameter Rayleigh number Ra_r is defined as $Ra_r = g\beta r_i^3 \Delta T/\alpha v$, and the Prandtl number Pr by $Pr = v/\alpha$, where β is the coefficient of thermal expansion and v the kinematic viscosity. Hereafter, the Rayleigh number $Ra = g\beta(r_o - r_i)^3\Delta T/\alpha v$ is employed for convenience in comparing the results to those of previous studies.

At the inner and outer cylinders, the components of velocity are zero and the components of vorticity follow from the definition of the vorticity vector. The vector potential boundary conditions are in agreement with the work of Hirasaki and Hellums [19], with the normal gradient of the normal component of vector potential specified as zero and the components of vector potential tangential to the surface also being zero. The dimensionless temperatures of the inner and outer cylinders are $\Theta = 1$ and $\Theta = 0$, respectively. Therefore, the dimensionless boundary conditions at $r = 1$ and $r = R$ are

$$\Omega_r = \frac{\partial}{\partial r}(r\Psi_r) = \Psi_\phi = \Psi_z = V_r = V_\phi = V_z = 0 \tag{11}$$

$$\Omega_\phi = -\frac{\partial V_z}{\partial r}, \quad \Omega_z = \frac{\partial V_\phi}{\partial r} \tag{12}$$

$$\Theta = 1 \text{ at } r = 1, \quad \Theta = 0 \text{ at } r = R \tag{13}$$

All of the numerical simulations were performed over the full radial, angular, and axial extent of the annulus. Simulations were first conducted using periodic boundary conditions at the lower vertical angular plane $\phi = \pi(-\pi)$ to demonstrate that the flow is symmetric about this plane for the ranges of R, Ra, and ω investigated. In subsequent simulations conducted within these ranges, symmetry boundary conditions (Eq. (14)) were employed only at $\phi = \pi(-\pi)$ for enhanced computational efficiency. It was confirmed that the results obtained using periodic boundary conditions at $\phi = \pi(-\pi)$ are the same as those from the corresponding cases with symmetry boundary conditions at $\phi = \pi(-\pi)$.

$$\Omega_r = \frac{\partial \Omega_\phi}{\partial \phi} = \Omega_z = \Psi_r = \frac{\partial \Psi_\phi}{\partial \phi} = \Psi_z = \frac{\partial V_r}{\partial \phi} = V_\phi = \frac{\partial V_z}{\partial \phi} = \frac{\partial \Theta}{\partial \phi} = 0 \tag{14}$$

At the adiabatic endwalls the components of velocity and the normal gradient of temperature are zero. Therefore, at $z = 0$ and $z = L$

$$\Omega_z = \Psi_r = \Psi_\phi = \frac{\partial \Psi_z}{\partial z} = V_r = V_\phi = V_z = \frac{\partial \Theta}{\partial z} = 0 \tag{15}$$

$$\Omega_r = -\frac{\partial V_\phi}{\partial z}, \quad \Omega_\phi = \frac{\partial V_r}{\partial z} \tag{16}$$

In the numerical simulations, it is assumed that the fluid is initially motionless, and the inner and outer cylinders, endwalls, and fluid are initially at the same uniform temperature of $\Theta = 0$. At $t = 0$, the temperature of the inner cylinder is suddenly increased to $\Theta = 1$. The flow patterns that subsequently develop in the annulus do so naturally as a result of transient heating of the fluid and the oscillation of the gravitational field. Numerical experiments were conducted using other types of initial conditions to determine their influence on the unsteady solutions. These included a purely conductive temperature field, and perturbed temperature fields corresponding to different orientations and directions of rotation of supercritical convective rolls. In each case, it was found that after a sufficient number of oscillations of the gravity field the unsteady solution was the same as that obtained using a quiescent and isothermal initial state. Therefore, no evidence was found that the final unsteady solution is dependent on the initial conditions.

Details of the numerical scheme employed in solving the system of non-linear governing equations (1)–(10) in conjunction with the boundary conditions (11)–(16), and a summary of comparisons of results to those of previous experimental and numerical studies to verify the accuracy of the numerical scheme are provided in Dyko and Vafai [17]. These comparisons show that the results from the present numerical algorithm are in excellent agreement with the experimental results of Dyko et al. [16] for air and a fluid with Prandtl number of 100, and the numerical results of Kuehn and Goldstein [20] and Cadiou et al. [21] for air. To ensure the results are not dependent on grid size or time step size, the extensive mesh and time step refinement procedures described in Dyko and Vafai [17] were also utilized in the present study.

2.2. Heat transfer

The angular mean Nusselt number is defined as the angular average of the local Nusselt number at the mid-axial plane, where the local Nusselt number is the ratio of the actual to conduction heat transfer. The expressions for the inner and outer cylinder angular mean Nusselt numbers $\overline{Nu}_{ai}$ and $\overline{Nu}_{ao}$, respectively, are

$$\overline{Nu}_{ai} = \frac{-1}{2\pi}\int_0^{2\pi} \ln(R)\frac{\partial \Theta}{\partial r}\bigg|_{r=1} d\phi \tag{17}$$

$$\overline{Nu}_{ao} = \frac{-1}{2\pi}\int_0^{2\pi} \ln(R)\frac{\partial \Theta}{\partial r}\bigg|_{r=R} d\phi \tag{18}$$

The time-averaged inner and outer cylinder angular mean Nusselt numbers $\overline{Nu}'_{ai}$ and $\overline{Nu}'_{ao}$ are obtained by integrating equations (17) and (18), respectively, over an integral number of periods of gravitational oscillation. The numerical simulations showed that after a sufficient number of oscillations of the gravitational field beyond $t = 0$, the minimum and maximum values of $\overline{Nu}_{ai}$ and $\overline{Nu}_{ao}$ no longer change as $\overline{Nu}_{ai}$ and $\overline{Nu}_{ao}$ oscillate in response to the gravitational oscillations. Once this situation is attained, $\overline{Nu}'_{ai}$ and $\overline{Nu}'_{ao}$ equal the same value which is reported herein as the time-averaged Nusselt number. This fact serves as a further check on the accuracy of the numerical scheme.

The time-averaged inner and outer cylinder overall Nusselt numbers are obtained by first integrating Eqs. (17) and (18), respectively, over the length of the annulus, and then over an integral number of periods of gravitational oscillation. After a sufficient number of oscillations of the gravitational field beyond $t = 0$, these Nusselt numbers equal the same value which is presented as the time-averaged overall Nusselt number.

3. Results

The unsteady flow and temperature fields in horizontal cylindrical annuli resulting from periodic modulation of the gravity field in a microgravity environment are presented. The effects of modulation frequency on the flow patterns, temperature distributions, and heat transfer are investigated for a large-gap annulus. The development of secondary flows that arise in moderate- and narrow-gap annuli owing to the onset of thermal instabilities, and the effects of frequency on heat transfer in moderate- and narrow-gap annuli are also studied. Comparisons are made between the results for microgravity and results for steady natural convection under terrestrial conditions.

Simulations were first conducted with oscillation amplitudes g' set to at least 100 times more than the constant gravity level g_o, which is typical of fluctuating accelerations on spacecraft. A second set of simulations was then performed using the same oscillation amplitudes as before, but with $g_o = 0.0$. The results for finite g_o were found to be essentially identical to those for $g_o = 0.0$, indicating that for each case studied the constant gravity level g_o has a negligible effect on the flow and temperature fields when $g' \geqslant 100 g_o$. Therefore, the results presented herein for $g_o = 0.0$ also apply to finite values of g_o when $g' \geqslant 100 g_o$, as is typical for spacecraft.

All of the numerical simulations were performed over the full radial, angular, and axial extent of the annulus as mentioned previously. The results of these simulations showed that the normal component of velocity and normal gradients of the tangential velocity components are zero at the mid-axial and vertical angular planes, owing to flow symmetry. Accordingly, the z-component of vector potential corresponds to the two-dimensional stream function at the mid-axial plane and the ϕ-component of vector potential corresponds to the two-dimensional stream function at the vertical angular plane.

The results of the simulations showed that, in a core region centered on the mid-axial plane of a sufficiently long large-gap annulus, the z-component of velocity is small and the temperature field is essentially unchanged with axial position. The streamlines and isotherms at the mid-axial plane presented in Section 3.1 for a large-gap annulus provide representative cross-sections of the flow and temperature fields in the core region. In moderate- and narrow-gap annuli, this core region does not exist at higher Rayleigh numbers owing to the inception of thermal instabilities which results in the formation of secondary flows. The simulations showed that secondary flows repeatedly form, dissipate, and re-form in the upper and lower regions of the annulus in response to the gravitational oscillations. The streamlines and isotherms at the vertical angular plane presented in Sections 3.2 and 3.3 for moderate- and narrow-gap annuli, respectively, provide representative cross-sections of the flow and temperature fields associated with the secondary flows.

The designation of low and high frequencies employed in this work is based on the frequency range over which flow patterns and heat transfer change appreciably. This occurs from approximately $\omega = 10$ to $\omega = 300$ as shown in the results. The periods of vibrations associated with these frequencies are generally small compared to the thermal and viscous characteristic times L_c^2/α and L_c^2/ν, respectively. Therefore, from a thermovibrational standpoint these can be considered high frequencies. It is noted for the parameters considered, the Nusselt number was found to oscillate with the frequency of the imposed oscillations.

3.1. Large-gap annulus

Simulations were performed for an annulus of radius ratio $R = 2.2$, dimensionless length $L = 10$, and peak Rayleigh number of $Ra = 10^4$, with air ($Pr = 0.7$) as the working fluid. To illustrate the effects of the frequency of the fluctuating gravitational field, results are presented for dimensionless frequencies of $\omega = 50$ and 200 for $g_o = 0.0$. The variation of the time-averaged Nusselt number over the frequency range $10 \leqslant \omega \leqslant 300$ is presented.

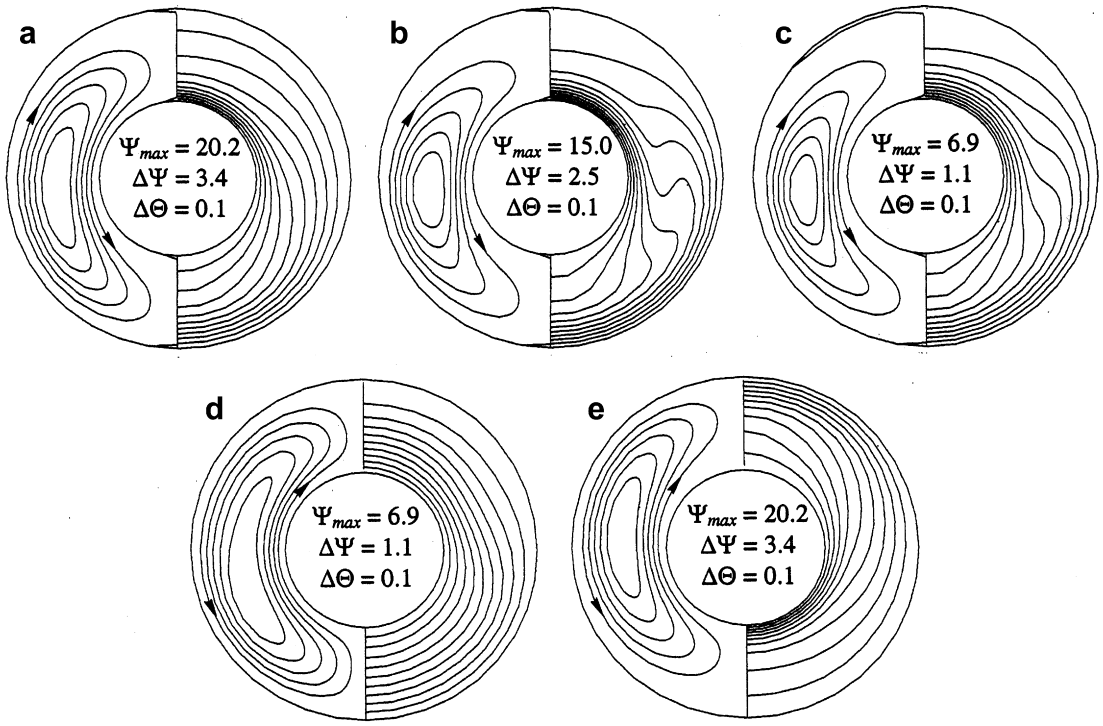

Fig. 2. Temporal response of streamlines and isotherms at the mid-axial plane over 1/2 the period of gravitational oscillation for $R = 2.2$, $L = 10$, $Ra = 10^4$, $Pr = 0.7$, $\omega = 50$, $\Delta t = \pi/200$: (a) $t = t_1$; (b) $t = t_1 + \Delta t$; (c) $t = t_1 + 2\Delta t$; (d) $t = t_1 + 3\Delta t$; (e) $t = t_1 + 4\Delta t$.

The temporal response of streamlines and isotherms at the mid-axial plane over a period of time π/ω (1/2 the period of gravitational oscillation) is presented on the left- and right-hand sides, respectively, of Fig. 2a–e for $\omega = 50$. The results shown in Fig. 2a correspond to a time $t = t_1$ when the instantaneous gravitational acceleration is $g = -g'$. The results in Fig. 2b–e correspond to times successively incremented from t_1 by $\Delta t = \pi/4\omega$ (1/8 the period of gravitational oscillation), when the instantaneous gravitational acceleration is $g = -g'\sin(\pi/4)$, 0, $g'\sin(\pi/4)$, and g', respectively. It is noted that, since the orientation of the gravitational vector was chosen to be downward, negative and positive values of g correspond to upward and downward gravitational accelerations, respectively.

At a time $t = t_1$ of maximum upward gravitational acceleration $g = -g'$, two crescent-shaped flow patterns with centers of rotation slightly below the horizontal angular plane are present in each of the axial planes within the core region. These patterns are symmetric to one another about the vertical angular plane. Since buoyancy forces act in the direction opposite of gravitational acceleration, the hotter fluid adjacent to the inner cylinder moves downward and the cooler fluid next to the outer cylinder moves upward, resulting in clockwise and counterclockwise recirculation on the left- and right-hand sides of the annulus, respectively. The isotherms are spaced more closely against the top of the inner cylinder and bottom of the outer cylinder, where the inner and outer cylinder thermal boundary layers are, respectively, thinnest. The characteristics of the flow and temperature fields are seen in the Fig. 2a plot of streamlines and isotherms at the mid-axial plane for $t = t_1$.

The flow and temperature fields change appreciably over the time period from $t = t_1$ to $t = t_1 + 2\Delta t$ as the magnitude of the upward gravitational acceleration decreases to zero. The crescent-shaped streamlines attain a less elongated appearance as seen in the sequence of Fig. 2a–c. Owing to the decreasing gravitational acceleration, the strength of the recirculating flow drops substantially as indicated by a reduction in the maximum value of stream function at the mid-axial plane from 20.2 at $t = t_1$ to 15.0 and 6.9 at $t = t_1 + \Delta t$ and $t_1 + 2\Delta t$, respectively. The isotherms become more closely grouped along the top of the inner cylinder and bottom of the outer cylinder over a time interval extending from $t = t_1$ to near $t = t_1 + \Delta t$, as the inner and outer cylinder thermal boundary layers continue to develop. Accordingly, the inner and outer cylinder angular mean Nusselt numbers increase over this interval, reaching a maximum value of $\overline{Nu}_{ai} = \overline{Nu}_{ao} = 1.95$. With further progression in time to $t = t_1 + 2\Delta t$, the isotherms become less closely grouped against the inner and outer cylinders owing to the continued reduction in strength of the flow, causing the Nusselt numbers to decrease. The changes in the isotherms from $t = t_1$ to $t = t_1 + 2\Delta t$ can be seen in Fig. 2a–c.

Over the time period from $t = t_1 + 2\Delta t$ (Fig. 2c) to $t = t_1 + 3\Delta t$ (Fig. 2d), dramatic changes in the flow and temperature fields occur as a result of reversal of the direction of gravitational acceleration. The recirculating flow reverses direction of rotation during this period, changing to counterclockwise and clockwise on the left- and

right-hand sides of the annulus, respectively. Following reversal of the flow, the heat transfer temporarily drops off to near that of pure conduction. This is evident from the isotherms plotted in Fig. 2d for $t = t_1 + 3\Delta t$, which are spaced much further from the top of the inner cylinder and bottom of the outer cylinder than at $t = t_1 + 2\Delta t$ (Fig. 2c), and appear as concentric arcs in the lower portion of the annulus. The inner and outer cylinder angular mean Nusselt numbers at $t = t_1 + 3\Delta t$ are near the minimum values of $\overline{Nu}_{ai} = 0.96$ and $\overline{Nu}_{ao} = 0.92$, respectively. The temporary drop-off in inner cylinder angular mean Nusselt number following flow reversal occurs because prior to this reversal much of the fluid in the lower part of the annulus is hot (Fig. 2c), and after flow reversal this fluid moves upward along the heated inner cylinder. Consequently, for a period of time following flow reversal the temperature difference between the inner cylinder and adjacent fluid remains small. Likewise, the outer cylinder angular mean Nusselt number temporarily drops off following flow reversal since most of the fluid in the upper portion of the annulus is relatively cold prior to reversal (Fig. 2c), and after reversal this fluid moves downward along the cooled outer cylinder.

With completion of 1/2 the period of gravitational oscillation at $t = t_1 + 4\Delta t$, the downward gravitational acceleration increases to the maximum value of $g = g'$. Owing to the increased strength of the recirculating flow and development of the thermal boundary layers, a more familiar crescent-shaped streamline pattern emerges and the isotherms become more closely grouped against the bottom of the inner cylinder and top of the outer cylinder, as seen in Fig. 2e. The streamlines and isotherms at $t = t_1 + 4\Delta t$ (Fig. 2e) appear as inverted images (rotated 180° about the horizontal line passing through $\phi = \pi/2$ and $-\pi/2$ at $z = L/2$) of those at $t = t_1$ (Fig. 2a), when the instantaneous gravitational acceleration is of equal magnitude but opposite direction. Additionally, the streamlines and isotherms at $t = t_1 + 5\Delta t$, $t_1 + 6\Delta t$, and $t_1 + 7\Delta t$ are inverted from those at $t = t_1 + \Delta t$, $t_1 + 2\Delta t$, and $t_1 + 3\Delta t$, respectively. After this, the temporal response of the streamlines and isotherms described up to this point is repeated every additional period of gravitational oscillation $8\Delta t$.

When the frequency of gravitational oscillation is increased to a sufficiently high value, the flow and temperature fields change significantly. This is apparent from comparing the temporal response of streamlines and isotherms at the mid-axial plane for $\omega = 200$ presented in Fig. 3 to that for $\omega = 50$ in Fig. 2. Note the time increment Δt is equal to $\pi/200$ for $\omega = 50$, and $\pi/800$ for $\omega = 200$. At times $t = t_1, t_1 + \Delta t$, and $t_1 + 2\Delta t$, the center of rotation of the recirculating flow is located above the horizontal angular plane for $\omega = 200$ and slightly below this plane for $\omega = 50$, as seen in Fig. 3a–c and 2a–c, respectively. After reversal of the flow, the center of rotation moves to below the horizontal angular plane for=200 (Fig. 3e) and slightly above this plane for $\omega = 50$ (Fig. 2e). The strength of the recirculating flow is generally much lower for $\omega = 200$ than for $\omega = 50$, as indicated by the maximum values of stream function at the mid-axial plane for $\omega = 200$ of 5.9, 10.3, 9.3, 3.9, and 5.9 at $t = t_1$, $t_1 + \Delta t$, $t_1 + 2\Delta t$, $t_1 + 3\Delta t$, and $t_1 + 4\Delta t$, respectively (compared to 20.2, 15.0, 6.9, 6.9,

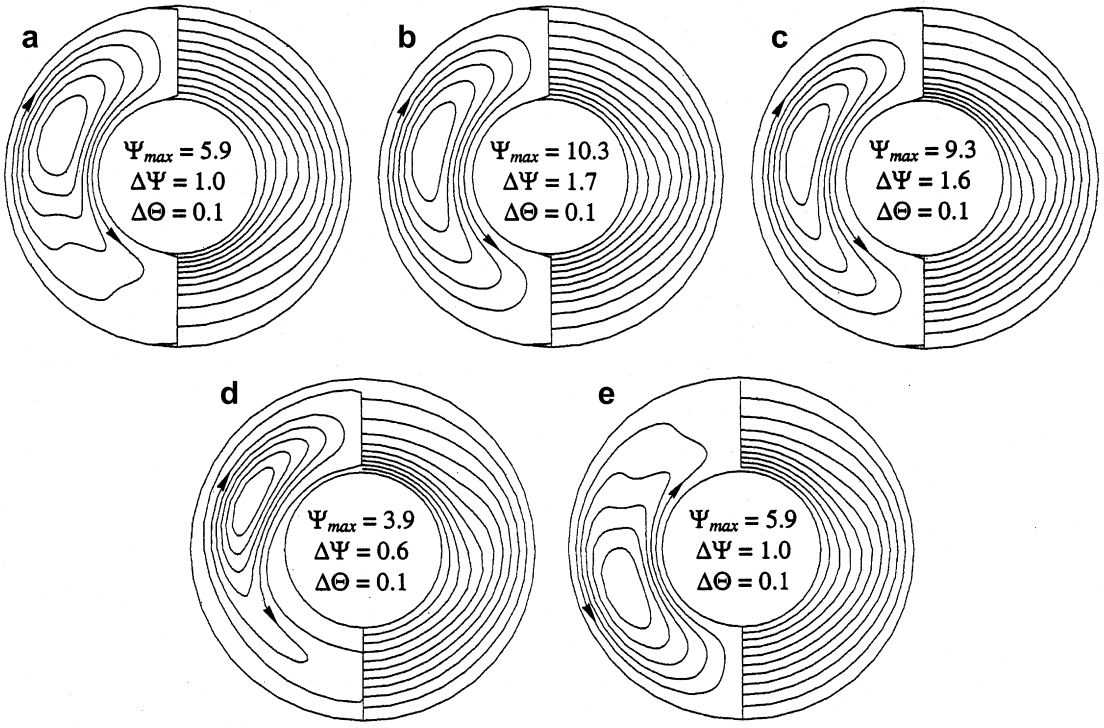

Fig. 3. Temporal response of streamlines and isotherms at the mid-axial plane over 1/2 the period of gravitational oscillation for $R = 2.2$, $L = 10$, $Ra = 10^4$, $Pr = 0.7$, $\omega = 200$, $\Delta t = \pi/800$: (a) $t = t_1$; (b) $t = t_1 + \Delta t$; (c) $t = t_1 + 2\Delta t$; (d) $t = t_1 + 3\Delta t$; (e) $t = t_1 + 4\Delta t$.

and 20.2, respectively, for $\omega = 50$). The isotherms change relatively little with time for $\omega = 200$ (Fig. 3a–e), in contrast to the more dramatic changes that occur for $\omega = 50$ (Fig. 2a–e). In general, the isotherms for $\omega = 200$ are spaced much more uniformly around the inner and outer cylinders than at $\omega = 50$. Owing to this relative lack of thermal boundary development for $\omega = 200$, the maximum instantaneous inner and outer cylinder angular mean Nusselt numbers are only $\overline{Nu}_{ai} = 1.12$ and $\overline{Nu}_{ao} = 1.09$, respectively, as compared to $\overline{Nu}_{ai} = \overline{Nu}_{ao} = 1.95$ for $\omega = 50$.

Simulations were performed for other frequencies in the range $10 \leqslant \omega \leqslant 300$ to obtain additional insight into the variation of Nusselt number with frequency. A plot of the time-averaged Nusselt number as a function of the parameter $1000\,\omega^{-2}$ over this frequency range is shown in Fig. 4. This plot illustrates the roll-off of Nusselt number as this parameter is decreased below a value of approximately 2.

It is seen in Fig. 4 that as the frequency is decreased from $\omega = 300$ to $\omega = 10$, the time-averaged Nusselt number increases from a value near 1.0 (indicating essentially no enhancement owing to convection) to a value of 1.65. The increase in time-averaged Nusselt number with decreasing frequency occurs as a result of the increase in time between flow reversals. At high frequencies there is insufficient time between flow reversals for significant development of the inner and outer cylinder thermal boundary layers, and the isotherms remain conductive in nature as seen in Fig. 3 for $\omega = 200$. At low frequencies, the time between flow reversals is greater and the thermal boundary layers become more fully developed. An indication of this is provided by the close grouping of isotherms next to the inner and outer cylinders as discussed previously for $\omega = 50$, and the appearance of the isotherms in Fig. 2b for $\omega = 50$ which is very similar to that for steady terrestrial natural convection as discussed later. Owing to the greater thermal boundary layer development at low frequencies, the peak values of the instantaneous angular mean Nusselt numbers $\overline{Nu}_{ai}$ and $\overline{Nu}_{ao}$ are much greater than those at high frequencies (as mentioned earlier for $\omega = 50$ compared to $\omega = 200$), and the time-averaged Nusselt number is also much greater than at high frequencies as seen in Fig. 4.

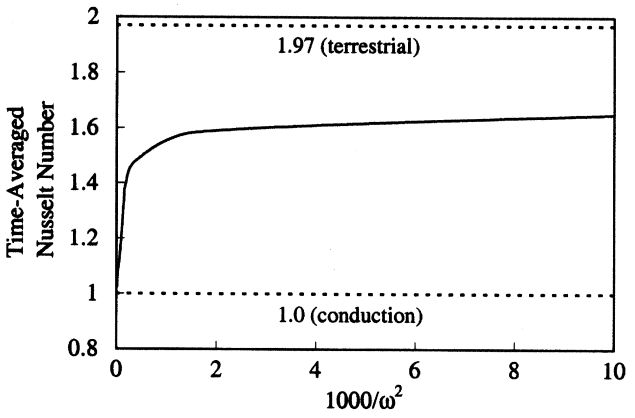

Fig. 4. Time-averaged Nusselt number for $R = 2.2$, $L = 10$, $Ra = 10^4$, $Pr = 0.7$ as a function of $1000/\omega^2$.

The streamlines and isotherms at the mid-axial plane for steady natural convection under terrestrial conditions (constant gravitational acceleration of magnitude $g = g'$) are plotted on the left- and right-hand sides, respectively, of Fig. 5a for $R = 2.2$, $L = 10$, and $Ra = 10^4$. The direction of the gravitational acceleration is downward in Fig. 5. The streamlines and isotherms at the mid-axial plane for $\omega = 50$ and $\omega = 200$ are plotted in Fig. 5b and c, respectively, for time $t = t_1 + 5\Delta t$ when the gravitational acceleration has remained downward for three time intervals $3\Delta t$ following the last gravitational reversal. By comparing Fig. 5b and c to Fig. 5a, it is seen that the streamlines and isotherms that arise between flow reversals become increasingly similar to those for terrestrial natural convection as the frequency of the gravitational oscillation is decreased. These trends are consistent with the results presented in Fig. 4, which show that the time-averaged Nusselt number becomes closer to the Nusselt number for terrestrial natural convection of 1.97 as the frequency is decreased from $\omega = 300$ to $\omega = 10$.

3.2. Moderate-gap annulus

Buoyancy-induced convection in an annulus with radius ratio $R = 1.6$ and dimensionless length $L = 3.6$ subjected to

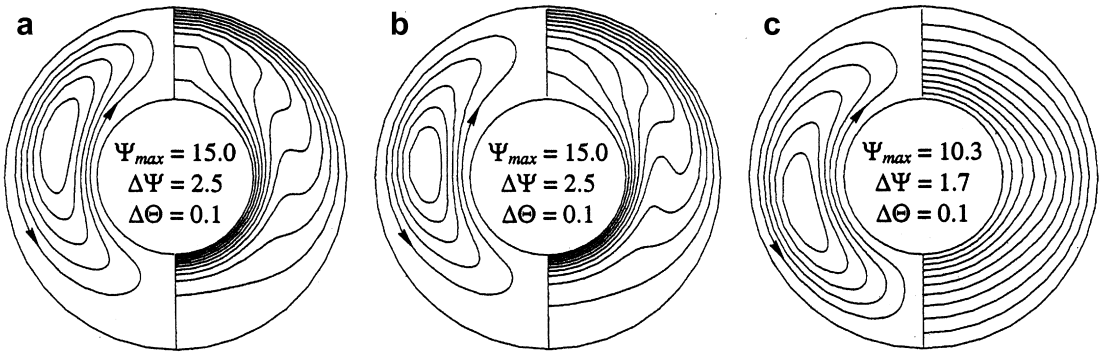

Fig. 5. Streamlines and isotherms at the mid-axial plane for $R = 2.2$, $L = 10$, $Ra = 10^4$, $Pr = 0.7$: (a) steady natural convection under terrestrial conditions (Dyko et al. [16]); (b) g-jitter under microgravity, $\omega = 50$, $t = t_1 + 5\Delta t$, $\Delta t = \pi/200$; (c) g-jitter under microgravity, $\omega = 200$, $t = t_1 + 5\Delta t$, $\Delta t = \pi/800$.

periodic gravity modulation in microgravity was investigated for air ($Pr = 0.7$). Simulations were conducted for a peak Rayleigh number of $Ra = 4.5 \times 10^3$, which permitted investigation of secondary flows that arise at Rayleigh numbers exceeding the critical value for instability of $Ra_c = 1.9 \times 10^3$ (Dyko et al. [16]), and for modulation frequencies in the range $25 \leqslant \omega \leqslant 300$.

The temporal response of streamlines and isotherms at the vertical angular plane is shown on the left- and right-hand sides, respectively, of Fig. 6a–e for $\omega = 50$. It is noted that the times at which results are presented in Fig. 6 for $R = 1.6$ and $\omega = 50$ are the same as those in Fig. 2 for $R = 2.2$ and $\omega = 50$. At the time $t = t_1$ of maximum upward gravitational acceleration $g = -g'$, the recirculating primary flow in the annulus is characterized by downward movement of the hotter fluid adjacent to the inner cylinder, and upward movement of the cooler fluid next to the outer cylinder. As seen in Fig. 6a, at this time a rotational cell is present in the lower portion of the moderate-gap annulus next to each endwall. The cells rotate in opposite directions, counterclockwise on the right-hand side of the annulus and clockwise on the left. These cells are actually cross-sections of transverse rolls (rolls with axes oriented in the angular direction) that extend across the lower region of the annulus. These transverse end rolls are driven by the primary flow and form because of the viscous shear imposed by the endwalls. The isotherms in the lower portion of the annulus are distorted at the endwalls owing to the presence of the end rolls. Between the end rolls, the axial velocity is very low and the isotherms are essentially independent of axial position. In the upper part of the annulus, the isotherms are slightly distorted near the endwalls owing to local retardation of the flow that results from the viscous shearing effect of the endwalls.

As the magnitude of the upward gravitational acceleration decreases to zero over the time period from $t = t_1$ to $t = t_1 + 2\Delta t$, some subtle but important changes in the streamlines and isotherms occur. From $t = t_1$ (Fig. 6a) to $t = t_1 + \Delta t$ (Fig. 6b), the streamlines between the end rolls in the bottom of the annulus become s-shaped and extend closer to the inner and outer cylinders indicating that supercritical transverse rolls have begun to form there. With further progression in time to $t = t_1 + 2\Delta t$ (Fig. 6c), however, these rolls fail to develop much further as evidenced by only small changes in the streamlines between the end rolls. Over the period from $t = t_1$ to $t = t_1 + 2\Delta t$, the strength of the end rolls first increases and then decreases, as indicated by the maximum values of stream function at the vertical angular plane of 1.1, 2.1, and 0.59 at times $t = t_1$, $t_1 + \Delta t$, and $t_1 + 2\Delta t$, respectively. This is reflected in the corresponding increase and subsequent reduction in distortion of the isotherms in the bottom of the annulus near the endwalls over this period (Fig. 6a–c).

Over the time period from $t = t_1 + 2\Delta t$ to $t = t_1 + 4\Delta t$ (which completes 1/2 the period of gravitational oscillation), the flow and temperature fields undergo significant changes owing to reversal of the direction of gravitational acceleration and the subsequent increase in magnitude of downward gravitational acceleration to the maximum value of $g = g'$. The recirculating primary flow in the annu-

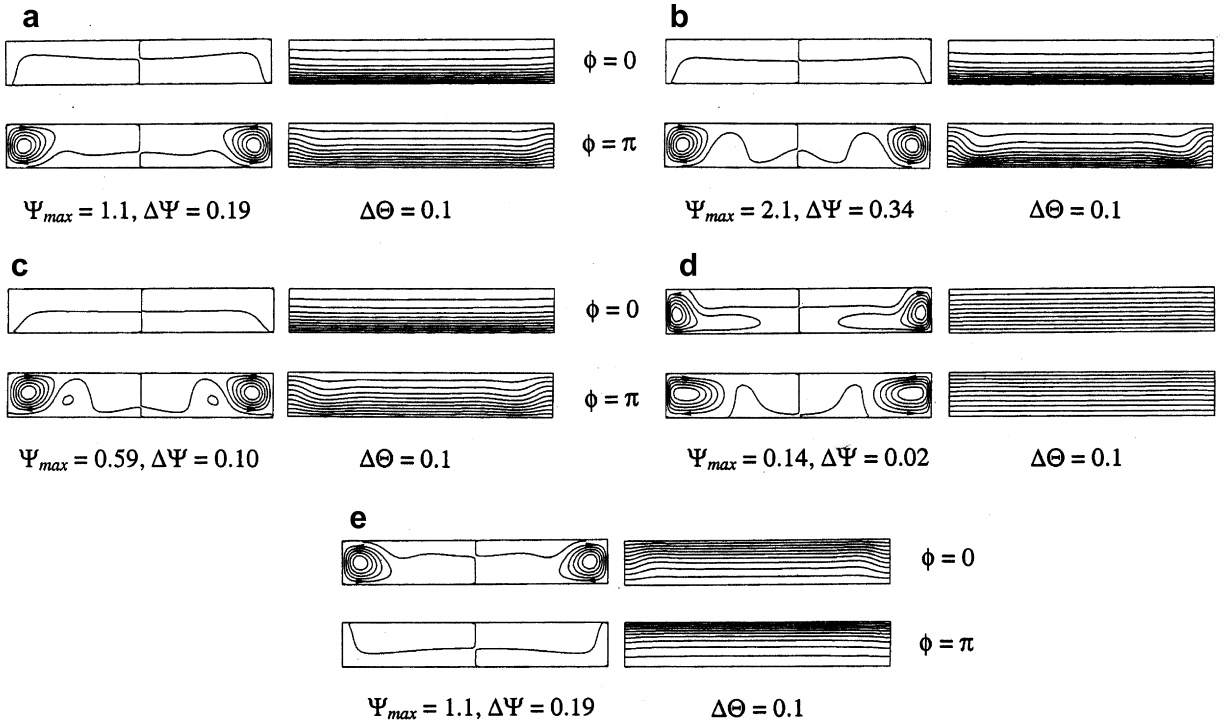

Fig. 6. Temporal response of streamlines and isotherms at the vertical angular plane over 1/2 the period of gravitational oscillation for $R = 1.6$, $L = 3.6$, $Ra = 4.5 \times 10^3$, $Pr = 0.7$, $\omega = 50$, $\Delta t = \pi/200$: (a) $t = t_1$; (b) $t = t_1 + \Delta t$; (c) $t = t_1 + 2\Delta t$; (d) $t = t_1 + 3\Delta t$; (e) $t = t_1 + 4\Delta t$.

lus reverses directions of rotation at a time between $t = t_1 + 2\Delta t$ and $t = t_1 + 3\Delta t$. As seen in Fig. 6d for $t = t_1 + 3\Delta t$ and Fig. 6e for $t = t_1 + 4\Delta t$, following this reversal a rotational cell forms in the upper portion of the annulus at each endwall, and the end rolls in the bottom of the annulus dissipate. The upper cells, which rotate clockwise on the right-hand side of the annulus and counterclockwise on the left, are cross-sections of transverse rolls that extend across the upper region of the annulus.

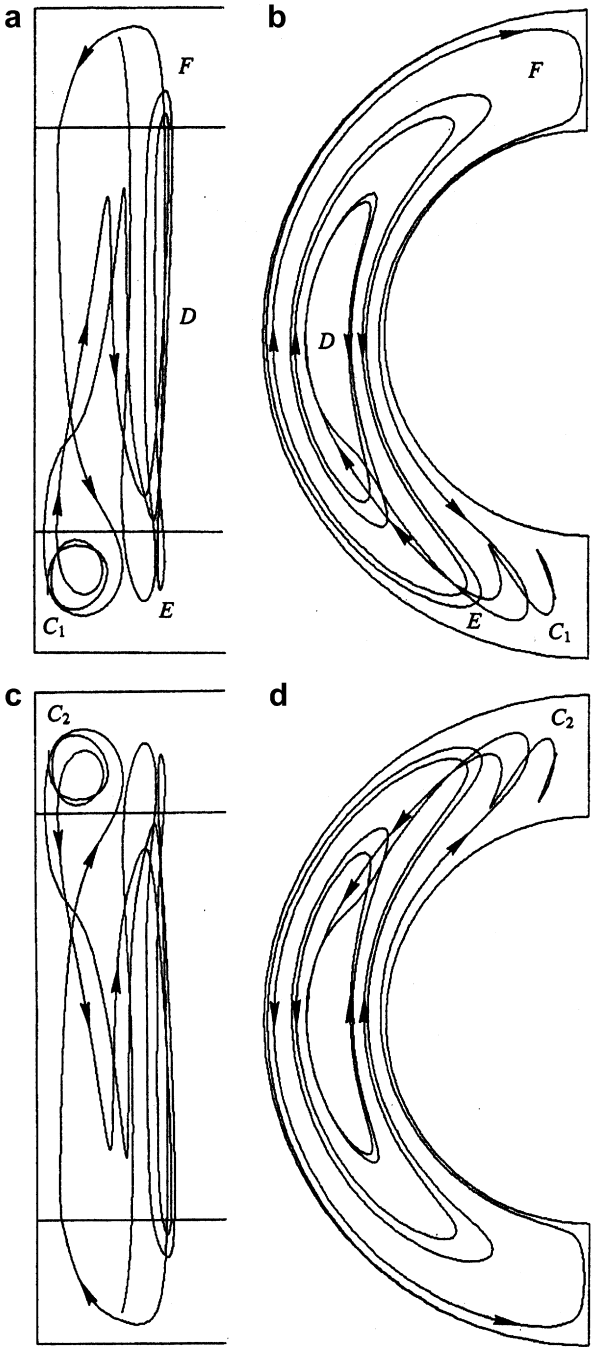

Fig. 7. Fluid particle path plots for $R = 1.6$, $L = 3.6$, $Ra = 4.5 \times 10^3$, $Pr = 0.7$: (a) side view of end roll region, $t = t_1 + 2\Delta t$; (b) end view of end roll region, $t = t_1 + 2\Delta t$; (c) side view of end roll region, $t = t_1 + 6\Delta t$; (d) end view of end roll region, $t = t_1 + 6\Delta t$.

As was the case for $R = 2.2$, for $R = 1.6$ the streamlines and isotherms at an instant in time are inverted from those present at times $4\Delta t$ earlier and later.

To better understand the three-dimensional nature of the flow, fluid particle path plots are presented in Fig. 7a and b for $t = t_1 + 2\Delta t$ and Fig. 7c and d for $t = t_1 + 6\Delta t$. The pathlines seen in Fig. 7a–d represent the trajectories of two massless particles injected into the flow fields. A single particle is released into a transverse roll in the lower part of the annulus (C_1), and another particle is released into a transverse roll in the upper part of the annulus (C_2). Note that these pathlines illustrate the structure of the flow at two different instances in time.

As seen in Fig. 7a and b, at $t = t_1 + 2\Delta t$ a particle injected into one of the transverse rolls (location C_1) follows a spiral trajectory transverse to the angular symmetry plane until becoming entrained in the primary flow. It then proceeds axially inward in a series of increasingly larger crescent-shaped helical patterns (region D) until it approaches the outer cylinder near the bottom of the annulus (location E). After this, it follows a route along the outer cylinder to the top of the annulus (location F), and moves axially outward before moving to the bottom of the annulus and becoming entrained in the transverse roll. The particle subsequently leaves the roll and proceeds along nearly the same path as before. It is seen in Fig. 7 that a particle introduced into a transverse roll in the lower part of the annulus at $t = t_1 + 2\Delta t$ (Fig. 7a and b) follows a path inverted from that of a particle released into the corresponding roll in the upper part of the annulus at $t = t_1 + 6\Delta t$ (Fig. 7c and d), when the instantaneous gravitational acceleration is of equal magnitude but opposite direction.

Streamlines and isotherms at the vertical angular plane for steady natural convection under terrestrial conditions are plotted on the left- and right-hand sides, respectively, of Fig. 8 for $R = 1.6$, $L = 3.6$, and $Ra = 4.5 \times 10^3$. From comparison of Fig. 6a–e to Fig. 8, it is seen that the supercritical inner transverse rolls that begin to form between the end rolls in the annulus subjected to gravity modulation under microgravity are much weaker than those that are prominently present under terrestrial conditions. Simulations were also conducted for modulation frequencies below $\omega = 50$ to determine the effect of frequency on development of the rolls. It was found that the supercritical inner rolls develop further at frequencies less than $\omega = 50$

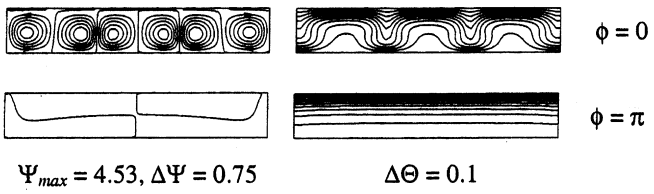

Fig. 8. Streamlines and isotherms at the vertical angular plane for $R = 1.6$, $L = 3.6$, $Ra = 4.5 \times 10^3$, $Pr = 0.7$: steady natural convection under terrestrial conditions.

owing to increased time between flow reversals, but still remain weaker than those associated with terrestrial natural convection. Therefore, from the results of the present study, it was found that gravity modulation has a stabilizing effect on the secondary flow compared to the case of constant gravitational acceleration, and this effect diminishes with reduced frequency.

The variation in time-averaged overall Nusselt number with the parameter $1000\,\omega^{-2}$ over the frequency range $25 \leqslant \omega < 300$ is shown in Fig. 9 for $R = 1.6$, $L = 3.6$, and $Ra = 4.5 \times 10^3$. Over this range, the time-averaged overall Nusselt number increases by $1.17 - 1.005 = 0.165$, which is 12 percent of the value for terrestrial natural convection of 1.41. As with the large-gap annulus (Fig. 4), the Nusselt number rolls-off at high frequencies. The Nusselt number again increases toward that for terrestrial natural convection as ω becomes smaller.

3.3. Narrow-gap annulus

Buoyancy-induced convection in an air-filled annulus with radius ratio $R = 1.1$ and dimensionless length $L = 0.7$ resulting from periodic gravity modulation in microgravity was studied. Simulations were performed for a peak Rayleigh number of $Ra = 2.5 \times 10^3$ which exceeds the critical value of $Ra_c = 1.74 \times 10^3$ (Dyko and Vafai [17]), thus permitting investigation of secondary flows, and for modulation frequencies in the range $25 \leqslant \omega \leqslant 300$.

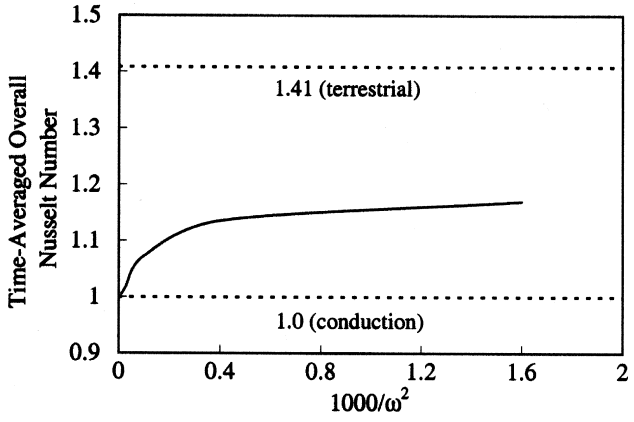

Fig. 9. Time-averaged overall Nusselt number for $R = 1.6$, $L = 3.6$, $Ra = 4.5 \times 10^3$, $Pr = 0.7$ as a function of $1000/\omega^2$.

The streamlines and isotherms at the vertical angular plane are shown on the left- and right-hand sides, respectively, of Fig. 10a–e for $\omega = 50$. The times at which results are presented in Fig. 10 for $R = 1.1$ and $\omega = 50$ are the same as those for $R = 1.6$ with $\omega = 50$ (Fig. 6), and $R = 2.2$ with $\omega = 50$ (Fig. 2). It is seen in Fig. 10a that at time $t = t_1$ (when the maximum upward gravitational acceleration is $g = -g'$), six counter-rotating cells are present in the lower part of the annulus. At this time, the recirculating primary flow exhibits downward movement of the hotter fluid adjacent to the inner cylinder, and upward movement of the cooler fluid next to the outer cylinder. Each of the six cells is a cross-section of a transverse roll that extends across the lower region of the annulus. The end rolls rotate counterclockwise on the right-hand side of the annulus and clockwise on the left-hand side. The supercritical inner rolls are slightly stronger than the end rolls, as indicated by the closer spacing of streamlines within the inner rolls. The alternating elevation and depression of isotherms along the length of the lower part of the annulus corresponding to the opposite direction of rotation of adjacent rolls is also seen in Fig. 10a.

Over the time period from $t = t_1$ to $t = t_1 + 2\Delta t$, the inner transverse rolls in the lower part of the annulus dissipate as the magnitude of the upward gravitational acceleration decreases to zero. This is seen in the plots of streamlines and isotherms provided in Fig. 10a–c for times $t = t_1$, $t_1 + \Delta t$, and $t_1 + 2\Delta t$, respectively. At $t = t_1 + 2\Delta t$, two very weak end rolls are present in the lower part of the annulus, and two similarly weak end rolls have formed in the upper part of the annulus. The isotherms in the upper and lower portions of the annulus appear as nearly straight lines which reflects the very low strength of the rolls. The maximum values of stream function at the verti-

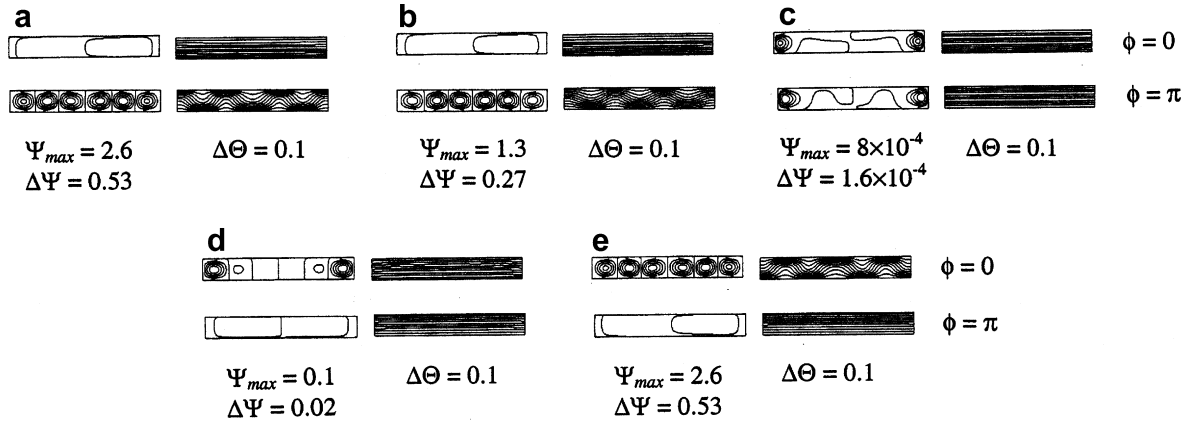

Fig. 10. Temporal response of streamlines and isotherms at the vertical angular plane over 1/2 the period of gravitational oscillation for $R = 1.1$, $L = 0.7$, $Ra = 2.5 \times 10^3$, $Pr = 0.7$, $\omega = 50$, $\Delta t = \pi/200$: (a) $t = t_1$; (b) $t = t_1 + \Delta t$; (c) $t = t_1 + 2\Delta t$; (d) $t = t_1 + 3\Delta t$; (e) $t = t_1 + 4\Delta t$.

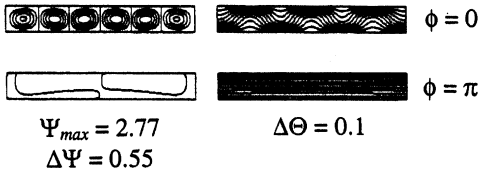

Fig. 11. Streamlines and isotherms at the vertical angular plane for $R = 1.1$, $L = 0.7$, $Ra = 2.5 \times 10^3$, $Pr = 0.7$: steady natural convection under terrestrial conditions (Dyko and Vafai [17]).

cal angular plane are 2.6, 1.3, and 8×10^{-4} at $t = t_1$, $t_1 + \Delta t$, and $t_1 + 2\Delta t$, respectively.

With further progression in time from $t = t_1 + 2\Delta t$ to $t = t_1 + 4\Delta t$ (completing 1/2 the period of gravitational oscillation), the direction of gravitational acceleration reverses and the downward gravitational acceleration increases to the maximum value of $g = g'$. The recirculating primary flow reverses directions of rotation. Over this time period, six counter-rotating rolls develop in the upper part of the annulus as seen in the sequence of Fig. 10c–e. The end rolls develop first, and then the supercritical inner rolls form, starting from the end rolls and progressing inward toward the middle of the annulus. The strength of the rolls increases dramatically over this period, as indicated by the maximum values of stream function at the vertical angular plane of 8×10^{-4}, 0.1 and 2.6 at times $t = t_1 + 2\Delta t$, $t_1 + 3\Delta t$, and $t_1 + 4\Delta t$, respectively. It is noted that once again, the streamlines and isotherms at any given time are inverted from those present at $\pm 4\Delta t$.

Results for steady natural convection under terrestrial conditions are plotted in Fig. 11 for $R = 1.1$, $L = 0.7$, and $Ra = 2.5 \times 10^3$. By comparing Fig. 10a–e to Fig. 11, it is seen that the supercritical transverse rolls which repeatedly form, dissipate, and re-form in the upper and lower portions of the annulus in response to the gravitational fluctuations under microgravity are very similar in appearance to the steady supercritical rolls that develop under terrestrial conditions. The maximum strength of the rolls is close to the roll strength for terrestrial natural convection, as indicated by the maximum values of stream function at the vertical angular plane of 2.6 for Fig. 10a and e and 2.8 for Fig. 11. In contrast to the moderate-gap annulus case for the same modulation frequency of $\omega = 50$ (Fig. 6), the supercritical inner transverse rolls in the narrow-gap annulus develop much further between flow reversals (Fig. 10), becoming close in strength and appearance to those present under terrestrial conditions. Therefore, it is apparent that the stabilizing effect of gravity modulation on supercritical flows diminishes as the annulus radius ratio R is reduced.

A plot of the time-averaged overall Nusselt number as a function of $1000\,\omega^{-2}$ over the frequency range $25 \leqslant \omega < 300$ is shown in Fig. 12 for $R = 1.1$, $L = 0.7$, and $Ra = 2.5 \times 10^3$. It is seen that over this range, the time-averaged overall Nusselt number increases by $1.03 - 1.004 = 0.026$, which is only 2 percent of the value for terrestrial natural convection of 1.09. By comparing these Nusselt number results to those for the moderate-gap

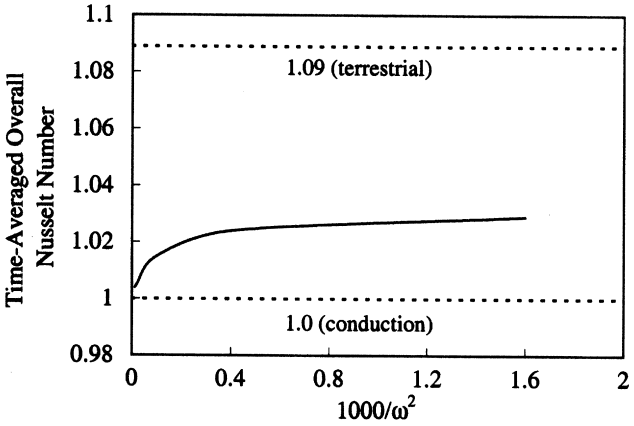

Fig. 12. Time-averaged overall Nusselt number for $R = 1.1$, $L = 0.7$, $Ra = 2.5 \times 10^3$, $Pr = 0.7$ as a function of $1000/\omega^2$.

annulus reported earlier, it is seen that the increase in time-averaged overall Nusselt number caused by reducing frequency becomes a smaller portion of the value for terrestrial natural convection as the annulus radius ratio R is reduced. The time-averaged overall Nusselt number exhibits a roll-off at high frequencies and tendency toward that for terrestrial natural convection at low frequencies, similar to those for large- and moderate-gap annuli (Figs. 4 and 9, respectively).

4. Conclusions

An investigation of buoyancy-driven convection in a cylindrical annulus subjected to gravity modulation in a microgravity environment has been conducted for the first time. Simulations were carried out for wide ranges of annulus radius ratio and modulation frequency. It was shown that the fluctuating gravitational field induces recirculating flows in the annulus that reverse direction of rotation in response to the gravitational reversals. At high frequencies, the strength of the flow remains relatively low and the flow and temperature fields are notably different than those associated with natural convection under terrestrial conditions. With reduction in frequency to lower values, the strength of the flow increases and the flow and temperature fields that arise between flow reversals become increasingly similar to those for terrestrial conditions. A distinguishing difference between the flow patterns at low and high frequencies is the position of the center of rotation of the flow relative to the horizontal angular plane. Except for a short period of time following flow reversal, at low frequencies the center of rotation is below and above this plane when the gravitational acceleration acts in the upward and downward directions, respectively. At higher frequencies the center of rotation is above and below this plane, respectively.

The results of the present study show that low frequency gravity modulation considerably enhances annulus heat transfer in a microgravity environment, as compared to the nearly pure conduction associated with either high frequency modulation or the absence of gravitational fluctua-

tions. At high frequencies, there is insufficient time between flow reversals for appreciable development of the inner and outer cylinder thermal boundary layers to occur. Consequently, heat transfer occurs essentially by conduction only. As the frequency is reduced, the time between flow reversals increases leading to further development of the thermal boundary layers, and heat transfer increases. For the large-gap annulus case that was studied, the time-averaged overall Nusselt number becomes a large fraction of the value for terrestrial natural convection as the frequency is decreased to low levels.

It was shown that secondary flows arise in moderate- and narrow-gap annuli subjected to gravity modulation under microgravity at sufficiently high Rayleigh numbers, owing to the inception of thermal instabilities. For a moderate-gap annulus at low frequency, supercritical transverse rolls begin to form between the end rolls following each flow reversal. This occurs in the upper and lower regions of the annulus when the direction of gravitational acceleration is downward and upward, respectively. The inner rolls develop slowly and remain weaker than those associated with terrestrial natural convection. In contrast to the moderate-gap annulus, at the same low frequency the supercritical inner rolls in a narrow-gap annulus develop much further following each flow reversal. For the narrow-gap annulus, rolls that are close in strength and appearance to those present under terrestrial conditions repeatedly form, dissipate, and re-form in the upper and lower regions in response to the gravitational fluctuations. It is concluded that gravity modulation has a stabilizing effect on the secondary flow compared to the case of constant gravitational acceleration, and this effect diminishes with reduction in annulus radius ratio R. This effect was also found to diminish with reduced modulation frequency. The increase in time-averaged overall Nusselt number resulting from reducing frequency was observed to become a smaller fraction of the value for terrestrial natural convection as R is reduced.

References

[1] W. Knabe, D. Eilers, Low gravity environment in Space-lab, Acta Astronautica 9 (1982) 182–198.
[2] Y. Kamotami, A. Prasad, S. Ostrach, Thermal convection in an enclosure due to vibrations aboard spacecraft, AIAA J. 19 (1981) 511–516.
[3] N. Amin, The effect of g-jitter on heat transfer, Proc. R. Soc. Lond. A 419 (1988) 151–172.
[4] S. Biringen, G. Danabasoglu, Computation of convective flow with gravity modulation in rectangular cavities, J. Thermophys. 4 (1990) 357–365.
[5] S. Biringen, L.J. Peltier, Numerical simulation of 3-D Bénard convection with gravitational modulation, Phys. Fluids A 2 (1990) 754–764.
[6] M.N. Cyr, A.N. Alexandrou, D.J. Olinger, Effects of gravity modulation in microgravity convection systems, ASME FED 171 (1993) 89–94.
[7] J.I.D. Alexander, S. Amiroudine, J. Ouazzani, F. Rosenberger, Analysis of the low gravity tolerance of Bridgman–Stockbarger crystal growth, II. Transient and periodic accelerations, J. Cryst. Growth 113 (1991) 21–38.
[8] H. Tang, Z.M. Tang, W.R. Hu, G. Chen, B. Roux, Numerical simulation of g-jitter effect on half floating zone convection under microgravity environment, Microgravity Sci. Technol. 9 (1996) 28–34.
[9] Y. Shu, B.Q. Li, H.C. DeGroh, Numerical study of g-jitter induced double-diffusive convection, Num. Heat Transfer A 39 (2001) 245–265.
[10] R.E. Powe, C.T. Carley, E.H. Bishop, Free convective flow patterns in cylindrical annuli, Trans. ASME, J. Heat Transfer 91 (1969) 310–314.
[11] Y.F. Rao, Y. Miki, K. Fukuda, Y. Takata, S. Hasegawa, Flow patterns of natural convection in horizontal cylindrical annuli, Int. J. Heat Mass Transfer 28 (1985) 705–714.
[12] Y. Takata, K. Iwashige, K. Fukuda, S. Hasegawa, Three-dimensional natural convection in an inclined cylindrical annulus, Int. J. Heat Mass Transfer 27 (1984) 747–754.
[13] T. Fusegi, B. Farouk, A three-dimensional study of natural convection in the annulus between horizontal concentric cylinders, Proceedings of the 8th International Heat Transfer Conference 4 (1986) 1575–1580.
[14] K. Vafai, J. Ettefagh, An investigation of transient three dimensional buoyancy driven flow and heat transfer in a closed horizontal annulus, Int. J. Heat Mass Transfer 34 (1991) 2555–2570.
[15] C.P. Desai, K. Vafai, An investigation and comparative analysis of two- and three-dimensional turbulent natural convection in a horizontal annulus, Int. J. Heat Mass Transfer 37 (1994) 2475–2504.
[16] M.P. Dyko, K. Vafai, A.K. Mojtabi, A numerical and experimental investigation of stability of natural convective flows within a horizontal annulus, J. Fluid Mech. 381 (1999) 27–61.
[17] M.P. Dyko, K. Vafai, Three-dimensional natural convective states in a narrow-gap horizontal annulus, J. Fluid Mech. 445 (2001) 1–36.
[18] M.P. Dyko, K. Vafai, On the presence of odd transverse convective rolls in narrow-gap horizontal annuli, Phys. Fluids 14 (2002) 1291–1294.
[19] G.J. Hirasaki, J.D. Hellums, A general formulation of the boundary conditions on the vector potential in three-dimensional hydrodynamics, Quart. Appl. Math. 26 (1968) 331–342.
[20] T.H. Kuehn, R.J. Goldstein, An experimental and theoretical study of natural convection in the annulus between horizontal concentric cylinders, J. Fluid Mech. 74 (1976) 695–719.
[21] P. Cadiou, G. Desrayoud, G. Lauriat, Natural convection in a narrow horizontal annulus: the effects of thermal and hydrodynamic instabilities, Trans. ASME, J. Heat Transfer 120 (1998) 1019–1026.